THE JOURNAL OF PHYSICAL CHEMISTRY B
A JOURNAL OF THE AMERICAN CHEMICAL SOCIETY

pubs.acs.org/JPCB

Article

QM/MM Simulations of Protein Crystal Reactivity Guided by MSOX Crystallography: A Copper Nitrite Reductase Case Study

Kakali Sen, Michael A. Hough, Richard W. Strange,* Chin Yong, and Thomas W. Keal*

Cite This: *J. Phys. Chem. B* 2021, 125, 9102−9114

Read Online

ACCESS | Metrics & More | Article Recommendations | Supporting Information

ABSTRACT: The recently developed multiple structures from one crystal (MSOX) serial crystallography method can be used to provide multiple snapshots of the progress of enzymatic reactions taking place within a protein crystal. Such MSOX snapshots can be used as a reference for combined quantum mechanical/molecular mechanical (QM/MM) simulations of enzyme reactivity within the crystal. QM/MM calculations are used to identify details of reference states that cannot be directly observed by X-ray diffraction experiments, such as protonation and oxidation states. These reference states are then used as known fixed endpoints for the modeling of reaction paths. We investigate the mechanism of nitrite reduction in an *Achromobacter cycloclastes* copper nitrite reductase crystal using MSOX-guided QM/MM calculations, identifying the change in nitrite binding orientation with a change in copper oxidation state, and determining the reaction path to the final NO-bound MSOX structure. The results are compared with QM/MM simulations performed in a solvated environment.

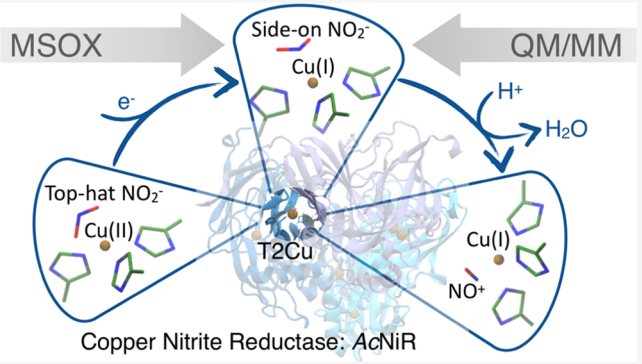

1. INTRODUCTION

Macromolecular crystal structures are usually obtained as single, static structures from one or more crystals, representing the average structure over the time duration of the experiment and over the X-ray exposed region of the crystal. Variable functional states of a protein or enzyme, such as its redox or ligand-bound states and the conformational changes associated with them, are typically analyzed by comparison of structures obtained from different crystals under sometimes differing experimental conditions.

The multiple structures from one crystal (MSOX) approach differs from "standard" crystallographic methods in that a series (tens to hundreds) of complete X-ray diffraction data sets are measured consecutively from the same volume of just one protein crystal.[1,2] Each exposure of the crystal to the X-ray beam produces a large number of solvated photoelectrons[3] from radiolysis of water molecules within the crystal, thus providing a source of reducing power to initiate catalytic reactions or other changes in the crystalline enzyme. In this manner, subsequent data sets from the dose series represent later stages of redox-driven reactions.

By solving a series of structures from these data sets, a structural "catalytic movie" is generated, so that a reaction mechanism or conformational change occurring in the crystal is obtained and is followed "*in crystallo*".[1,4] Metal redox states cannot be identified unambiguously from X-ray structures alone, and in situ single-crystal spectroscopy (e.g., UV−vis and/or resonance Raman)[5−7] can be interleaved with MSOX data collection where appropriate, to aid identification of the redox and ligand-bound states before and after exposure to X-rays during the series. A schematic of the MSOX approach is shown in Figure 1. Recent developments in beamline and X-ray detector technologies[8] and software, along with cluster-computing resources to autoprocess high-throughput data, have made the MSOX method practicable within a reasonable amount of experimental time. For example, a complete diffraction data set can now be collected using <1 s per complete data set, so that a 100 data set series can be collected in ∼15 min (allowing for instrumental deadtime). Low X-ray doses should be used to enable extended MSOX series to be collected before a loss of diffracting power and resolution through radiation damage becomes prohibitive. This approach relies on site-specific (e.g., redox) changes to the enzyme at the metal-containing active sites occurring at far lower absorbed X-ray doses than those which cause "global" radiation damage such as loss of diffracting power.[9−11] For example, we recently collected a series of 75 data sets (resolution 1.08−1.84 Å) at 190 K from one crystal of *Achromobacter cycloclastes* copper nitrite reductase (*Ac*NiR) and a series of 20 data sets (resolution 1.4−1.9 Å) at room temperature[a] from a similar

Received: April 23, 2021
Revised: July 8, 2021
Published: August 6, 2021

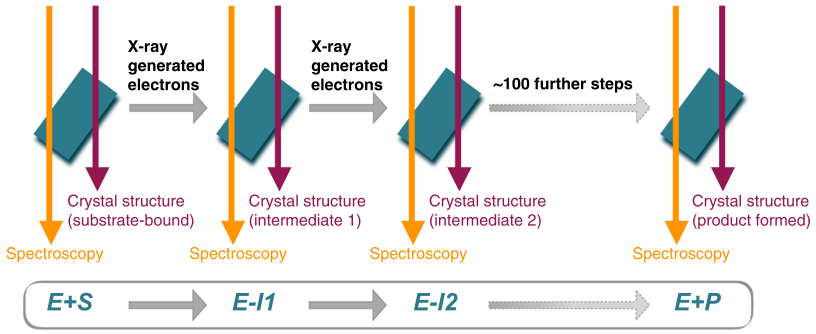

Figure 1. Multiframe "structural movie" using multiple structures from one protein crystal (MSOX). X-rays generate electrons within protein crystals that will migrate to redox centers and initiate and drive enzyme catalytic cycles (controlled radiolysis), from the initial state (E + S) to the final state (E + P) via intermediate states (E-I1, E-I2, etc.); each of which is structurally characterized at atomic to high resolution. Enzyme states generated in this way are representative of those in vivo, where the electrons that drive reactions are provided by biological electron transfer. Crystal spectroscopies are used to help unambiguously assign the serial structures to relevant states of the enzyme mechanism.

crystal.[12] Very recent data has extended this method to microcrystals at room temperature.[2]

The reactivity of complex chemical systems such as enzymes can be simulated using hybrid quantum mechanical/molecular mechanical (QM/MM) modeling. In a QM/MM calculation of an enzyme, the active site is modeled using an electronic structure method such as density functional theory (DFT) to correctly describe the chemical reaction that takes place there. For the surrounding environment, which does not directly participate in the reaction but may influence it indirectly, it is sufficient to use a classical molecular mechanical force field. The QM/MM approach ensures that computational resources are used efficiently by limiting the size of the QM calculation while retaining the higher accuracy of the QM description where it is needed and has been applied to a wide range of biomolecular systems.[13]

QM/MM calculations of enzymes are typically set up based on a single initial structure derived by macromolecular crystallography, to which missing elements such as hydrogen atoms, unobserved amino acid side chains, and protonation states are added.[14] The whole system is then solvated and equilibrated using classical molecular dynamics (MD) to represent the natural environment. Once equilibrated, several "snapshots" are taken from the MD trajectory and optimized at the QM/MM level,[15] which can be used as a starting point for exploring reaction mechanisms, calculating transition-state barriers, and so on. In this paper, we describe how the additional information provided by MSOX crystallography can be used to guide QM/MM simulations to form a complete picture of a redox reaction taking place in a crystal. Each structure in the conceptual MSOX series depicted in Figure 1 is a potential experimentally validated starting point for QM/MM calculations. QM/MM can be used to determine how the system evolves from one MSOX structure to the next, including analysis of preferred oxidation and protonation states at each point and reaction paths between them. QM/MM can further be used to simulate the equivalent reaction in a solvated environment (snapshots taken from the MD trajectory initiated from MSOX structures) to determine the enzyme's behavior in nature and how well the reaction that takes place in the crystal corresponds to this. Furthermore, QM/MM can provide key insights into the challenging problem of how best to interpret and model experimentally derived electron density maps.

We perform MSOX-guided QM/MM simulations for the case of a two-domain copper nitrite reductase (CuNiR) from *A. cycloclastes* (*Ac*NiR). CuNiRs are enzymes occurring in a wide range of denitrifying bacteria and fungi and they perform a vital role in the denitrification pathway of the nitrogen cycle.[16] Denitrification is a process critical for regulating the amount of biological nitrogen in the soil and in returning fixed nitrogen gas to the atmosphere. This is realized through the enzymatic reduction of nitrate or nitrite to the nitrogen gas product via nitric oxide and nitrous oxide intermediates.[17] The first irreversible reaction that commits the organism to generation of the final product is the reduction of nitrite to nitric oxide ($NO_2^- + e^- + 2H^+ \rightarrow NO + H_2O$), a reaction performed by either Fe-containing cytochrome *cd1* NiRs, pentaheme or octaheme NiRs, or by CuNiRs.[18]

The functional core of CuNiRs consists of two different Cu sites: the T1Cu site is responsible for accepting an electron from an external redox partner and transferring it to the second T2Cu site via the Cys-His bridge (Figure 2). The T2Cu site is

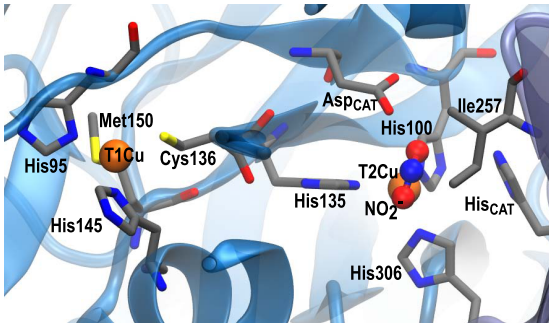

Figure 2. T1Cu and T2Cu sites and surrounding residues in *A. cycloclastes* nitrite reductase.

the catalytic site where NO_2^- binds and reduction occurs. The properties of CuNiRs have been extensively studied, and structural insights into enzyme function and the catalytic mechanism have recently been reviewed.[18] Two non-Cu coordinating residues have been implicated in proton transfer around the T2Cu pocket with an additional hydrophobic residue involved in substrate specificity. In *Ac*NiR, these are residues Asp98 and His255, referred to hereafter as Asp_{CAT} and His_{CAT}, and Ile257.

Several DFT studies have previously been carried out to understand the mechanism of nitrite reduction in CuNiRs in

https://doi.org/10.1021/acs.jpcb.1c03661
J. Phys. Chem. B 2021, 125, 9102−9114

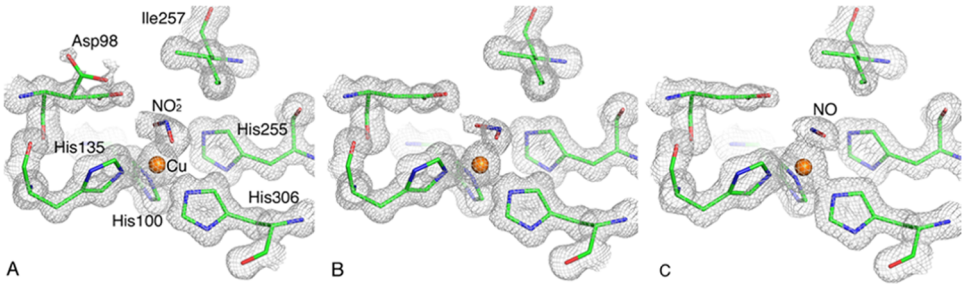

Figure 3. Three intermediate T2Cu ligand-bound structures selected for QM/MM from the experimental MSOX series measured from the same *Ac*NiR crystal at 190 K. These are (A) top-hat ds1 (PDB 5OF5) and (B) side-on ds2 (PDB 5OF6) orientations of NO_2^- and (C) the product side-on NO in ds18 (PDB 5OF8). The 2Fo-Fc electron density maps are contoured at 0.57, 0.55, and 0.42 electrons/Å^3, respectively.

an attempt to corroborate experimental observations. There have been several proposals related to an orientation change of nitrite from O-bound to N-bound on reduction, modulation of nitrite binding and reduction depending on the protonation state of Asp_{CAT} and His_{CAT}, and the ordering of reduction of Cu(II) at the T2Cu site vs proton transfer.[19−22] Lintuluoto and Lintuluoto further extended their DFT studies to hybrid QM/MM including both T1Cu and T2Cu sites to study protonation effects on intraelectron transfer in NiR from *Geobacillus thermodenitrificans*[23] (*Gt*NiR). They concluded that interprotein electron transfer to T1Cu is independent of nitrite binding; however, intraelectron transfer required protonation of His244 (equivalent to His_{CAT}) that corroborated photolysis experiments implying pH dependence of the reduction potential of the T2Cu site. Additionally, their calculations revealed that nitrite reduction involves proton transfer from His244 to Asp98 via the water bridging these residues, and the protonation of these residues in turn is controlled by the proton pool, a cluster of three water molecules, near His244. This proton pool in *Gt*NiR is created by the presence of Val249 that blocks the second solvent channel common in CuNiRs that links His_{CAT} to bulk solvent.[24,25] A recent neutron crystallography structure of *Ac*NiR in its resting state[26] suggests different protonation states (deprotonated Asp_{CAT} and His_{CAT}) for these catalytic residues, and hence, a complete understanding of the nitrite reduction mechanism remains elusive.

In Section 2, we summarize the experimental MSOX data that is used to guide QM/MM simulations in the crystal. The computational details of QM/MM simulations are provided in Section 3 as applied to the mechanism of nitrite reduction at the T2Cu catalytic site in *Ac*NiR. In Section 4, we present the results of QM/MM simulations in both the crystal and solvated environments and compare the two types of simulations in Section 5.

2. MSOX REFERENCE DATA

The starting point for MSOX-guided QM/MM simulations is a measurement of the experimental MSOX data. The experimental methodology to achieve this has been previously described in detail[1,12] and is only summarized briefly here and in Figure 1. A low-dose X-ray crystallographic data set is measured from a single suitably mounted crystal maintained at a selected temperature (e.g., 100, 190 K, or at ambient temperature). Previous work has shown that the response of the enzyme *in crystallo* to X-ray-induced redox changes is greater with elevated temperatures as greater dynamic freedom is present, although this must be balanced against a faster progression of global radiation damage and loss of diffracting power as the temperature increases.[12] The conditions of the initial data set collection should be chosen such that sufficient resolution is achieved to provide an accurate structure of the active site while minimizing the X-ray-induced changes from the "pristine" starting structure. A series of further data sets are measured, with the option of interleaving spectroscopic data collection from the crystal to monitor (where a suitable chromophore is present) the progress of the enzymatic reaction. It is often useful to increase the X-ray dose per data set later in the MSOX series to compensate for the loss of diffraction power through global radiation damage. The MSOX experiment is generally ended when the resolution of the data sets being produced falls below that required to effectively model the active site (which is crystal/enzyme dependent, but typically ca. 2 Å depending on which structural features related to the mechanism are to be resolved). The MSOX data sets are then processed in a consistent manner, and the structures refined appropriately.

The MSOX data for this study were taken from the series measured at 190 K.[12] The starting structure of the series (data set 1) represents a very low dose, close to the intact structure of the Cu(II)−nitrite enzyme-substrate complex. Subsequent frames capture the conversion of nitrite to the product NO in a side-on binding geometry, followed by dissociation of NO from the active site and rebinding of water to re-form the T2Cu−H_2O resting state. A total of 75 data sets were measured from the same crystal, with the resolution varying from 1.08 Å in data set 1 to 1.84 Å in data set 75.

The intermediates observed along the series are summarized in Figure 3 and distinctly show a dose-dependent orientation change of NO_2^- in the active site and its reduction to the reaction product NO. The first intermediate (Figure 3A) corresponding to the first data set (ds1) shows a top-hat orientation of nitrite bound to T2Cu, followed by switching to a side-on NO_2^- orientation (Figure 3B) in the second data set (ds2). In situ spectroscopic measurements taken during the MSOX experiment[12] indicated that the T1Cu site is largely reduced by ds2 and almost fully reduced in data set four (ds4), which still corresponds to a side-on NO_2^--bound T2Cu species. These states are followed by observation of a mixture of NO_2^- and NO and then by the complete formation of the side-on NO product (Figure 3C) complex by data set 18 (ds18). Next to follow after a prolonged dose lag (to ds50) is a replacement of NO with water, taking the enzyme back to its resting T2Cu-OH_2 state. Both the MSOX data and our previous DFT calculations[27] indicate that the two orientations of nitrite at the T2Cu site are related to the oxidation states of T2Cu. As it is not straightforward to assign the redox state of the metal and protonation of the catalytic residues from the

https://doi.org/10.1021/acs.jpcb.1c03661
J. Phys. Chem. B 2021, 125, 9102−9114

electron density maps, here we combine them with QM/MM calculations on these MSOX structures to produce a complete description of the reduction pathway catalyzed by CuNiR.

3. COMPUTATIONAL METHODS

3.1. QM/MM Modeling of Crystal Reactivity Based on MSOX Structures. We have performed QM/MM simulations to model the mechanism of nitrite reduction as it takes place in the crystal, using experimentally observed protein geometries. The aim of this is to establish a direct correspondence to MSOX experimental structures, such that QM/MM calculations can supply experimentally inaccessible information, such as protonation and oxidation states, and explore reaction paths between the observed MSOX structures, thus giving a complete picture of reactivity in the crystal.

Three observed intermediate crystal structures in the AcNiR mechanism were selected from the 190 K MSOX data series:[12] two distinct NO_2^- intermediates (top-hat and side-on binding modes to T2Cu), and the product T2Cu−NO complex[b]. The structures were prepared for simulations by removing all double occupancy mainchain and side-chain atoms and partial water molecules, keeping those with greater fractional occupancy or lower B-factors. The homotrimeric biological unit was generated from the clean version by applying symmetry operations to the single *Ac*NiR monomer of the crystallographic asymmetric unit. Note that to limit the overall computational expense of the calculation, we have not modeled the packing of the homotrimeric unit and so longer range interprotein interactions are omitted; we do not however expect that this approximation will significantly affect the detailed behavior of the reaction at the active site. The protonation states of the titratable residues were adjusted to be consistent with pH 5, the pH condition for crystallization of *Ac*NiR, using the propKa module[28,29] of the PDB2PQR suite of programs,[30] followed by visual inspection of the local side-chain environments. Once the pH was set, the PDB2PQR suite of programs was used to add hydrogen atoms as appropriate to the protein. All ionizable residues were in their standard protonation states, with histidine residues either singly protonated at N^{δ} (26, 100, 135, 306) or N^{ϵ} (95, 145, 260) or doubly protonated (28, 60, 76, 217, 231, 245, 319), except for Asp_{CAT} and His_{CAT} whose protonation states were varied as discussed below. Previous work from Ghosh et al.[31] supports protonation of both Asp_{CAT} and His_{CAT} at pH 5.0, and we focus on this state in this manuscript, which we refer to as Asp98p-Hsp. Recent neutron crystallography results, however, indicate that the resting state of *Ac*NiR is deprotonated (at pD 5.4) at both Asp_{CAT} and His_{CAT}.[26] The authors proposed that after binding of nitrite, Asp_{CAT} becomes protonated by proton transfer from the water molecule found bridging between Asp_{CAT} and His_{CAT}. As the true protonation states in nitrite-bound *Ac*NiR have not yet been experimentally demonstrated, we have also considered alternative protonation states of the Asp_{CAT} and His_{CAT} pair: only His_{CAT} protonated, which we denote as Asp98-Hsp, and only Asp_{CAT} protonated, which is referred to as Asp98p-Hsd, with results provided in the Supporting Information (SI). The water molecules present in the crystal structure were retained, and the structures were subjected to minimization to optimize H-atom positions while maintaining the heavy atoms fixed to their crystallographic coordinates. Once minimized, the structures were ready for use in the QM/MM studies.

In our QM/MM partitioning scheme, the QM region consists of the three histidine residues coordinating the T2Cu center (His100, His135, and His306), the NO_2^- ligand, the three critical active site residues, Asp_{CAT}, His_{CAT}, and Ile257, and any water molecules immediately H-bonded to Asp_{CAT}, His_{CAT}, and the NO_2^- ligand.[27] In all of the MSOX intermediates, in the active site, a water molecule bridges His_{CAT} to Asp_{CAT} via H-bonding and is the only water residue considered in the QM region. The residues were truncated at the neutral $C\alpha-C\beta$ bond and were capped with H-atoms to satisfy the valency for QM calculations. Atoms within 4 Å of the QM region were relaxed during QM/MM geometry optimizations, while the remaining atoms were frozen. The size of the unconstrained region was restricted to a small 4 Å window to allow one or more layers of water or amino acid residues to be fixed to prevent any large movement of outer atoms to the vacuum, which would give erroneous results.

QM/MM calculations were performed with the Tcl-based version of the ChemShell computational chemistry environment,[32,33] using ORCA[34] and DL-POLY[35] for the density functional theory and molecular mechanics calculations, respectively, and the DL-FIND module for geometry optimizations.[36] The electrostatic embedding scheme with charge shift correction was used to represent the surrounding MM partial charge distribution. The density functional B3LYP[37,38] with the DFT-D3 dispersion correction[39] was used for QM atoms during geometry optimization, and def2-SVP basis sets were used for all QM atoms except Cu, which was treated with the def2-TZVP basis set.[40] Further calculations were performed using the functionals PBE, PBE0, and B2PLYP for comparison. The CHARMM36 force field[41] was used for the MM region. Thermal and entropic corrections to the optimized minima were determined in DL-FIND from numerical vibrational frequency analyses. The climbing image nudged elastic band (CI-NEB) method[42] implemented in DL-FIND was used to calculate minimum energy paths between the optimized monodentate top-hat nitrite-T2Cu(I) and the other observed intermediate (N-bound, reverse side-on, and side-on) nitrite-T2Cu(I) structures. To ensure a consistent energy surface, all of the atoms that were kept flexible in the QM/MM optimization were optimized while all other atoms were fixed, and the same functional and basis sets were used as for endpoint minimizations. The transition states identified by the CI-NEB calculations in the MSOX-guided reaction pathway were further optimized using the dimer method[43] implemented in DL-FIND to obtain refined reaction barriers.

3.2. QM/MM Modeling of Reactivity in the Solvated Environment. For comparison with the crystal reaction, we have also performed conventional solvated QM/MM simulations which aim to reproduce in vivo conditions. These start from the first data set in the experimental series, which in this study is a top-hat NO_2^--bound MSOX structure. In contrast to the crystal simulations, the solvated system is equilibrated using classical molecular dynamics and snapshots are taken as the starting point for QM/MM optimizations. The subsequent intermediates in the reaction are also located starting from the initial top-hat NO_2^--bound QM/MM snapshots, to avoid forcing the system to take an identical reaction path to the crystal, as this may not be justified in a different environment. In the solvated system, however, besides the water molecule that bridges the His_{CAT} to Asp_{CAT} via H-bonding, any water molecules immediately H-bonded to Asp_{CAT}, His_{CAT}, and the

https://doi.org/10.1021/acs.jpcb.1c03661
J. Phys. Chem. B 2021, 125, 9102−9114

NO_2^- ligand[27] are considered in the QM region. The solvated QM/MM calculations are otherwise performed in an analogous way to those in the crystal, and the results compared to judge the effect of the environment on the mechanism of nitrite reduction.

The Asp98p-Hsp structure used for crystal simulations was solvated by padding a 15 Å layer of TIP3P water[44] in all three directions using a pre-equilibrated cubic water box available via the solvate plugin module within VMD.[45] Six chloride counterions were added after solvating the protein to maintain the electroneutrality of the simulation models using the autoionization feature in VMD. Explicit all-atom MD simulations were performed on these systems using NAMD 2.9[46] with the CHARMM36 force field. These simulations employed Langevin dynamics with periodic boundary conditions at 293 K. Long-range electrostatics were treated by the Particle Mesh Ewald method. The cutoff for nonbonded parameters is set at 12 Å with a smooth switching function turned on from 10 Å. In NPT simulations, the pressure was maintained with the Langevin piston method. Both the systems were initially subjected to 5000 steps of conjugate gradient (CG) minimization to eliminate any unphysical contacts. Then, the water and ions were equilibrated in an NVT ensemble, keeping the protein fixed for 1 ns. This was followed by 5000 steps of CG minimization and 5 ns equilibration under an NPT ensemble keeping the backbone harmonically restrained (5 $kcal^{-1}$ mol^{-1} $Å^2$) and the coordination spheres of both the T1Cu and T2Cu sites (comprised of the side chains of $(His)_2(Met)(Cys^-)$ and $(His)_3(NO_2^-)$, respectively) constrained at their crystallographic coordinates. The nonbonding (charges and van der Waals) parameters used for the T1Cu and T2Cu sites were the same as used in our previous work.[27] The simulation was continued for another 25 ns after removing backbone restraints but maintaining the constraints for the T1Cu and T2Cu sites.

Snapshots were taken from the equilibrated MD trajectory as a starting point for QM/MM optimizations. The MD trajectory was analyzed, and six different orientations based on water interaction with NO_2^- and Asp_{CAT}, and the positions of His_{CAT} and Ile257, were chosen. A water shell of 7 Å surrounding the protein was cut to derive solvated systems for QM/MM calculations. All residues with any atoms within 7 Å of the QM region were relaxed during QM/MM geometry optimizations while the remaining atoms were frozen. QM/MM energy and gradient evaluations of the solvated system were performed using the same level of theory as in the crystal to ensure the resulting structures and mechanisms could be compared.

Further calculations were prepared for the Asp98-Hsp and Asp98p-Hsd systems in the same manner for comparison.

4. RESULTS

4.1. Nitrite Binding in Crystalline *Ac*NiR. *4.1.1. Snapshot 1: Top-Hat Orientation of NO_2^-.* The first observed structure of NO_2^- bound to T2Cu is the "top-hat" orientation, where NO_2^- is ligated to T2Cu with the two oxygen atoms equidistant to T2Cu and a longer Cu−N distance (Figure 3A). Since the resting state of Cu in the enzyme is assigned to be in the Cu(II) state, and this was corroborated by our previous DFT calculations, we first considered the Cu(II) state for calculations on the top-hat intermediate. The Cu(II) state was studied for two alternative positions of top-hat NO_2^--bound structures, as seen in MSOX structures. As described in the Computational Methods section, the focus of this study is the Asp98p-Hsp system, although different protonation states of Asp_{CAT} and His_{CAT} are taken into account where relevant.

Optimization of T2Cu in the Cu(II) oxidation state always resulted in a bidentate top-hat orientation, independent of the protonation state of Asp_{CAT} and His_{CAT} or the initial MSOX structure. Figure 4 shows the MSOX and calculated structures

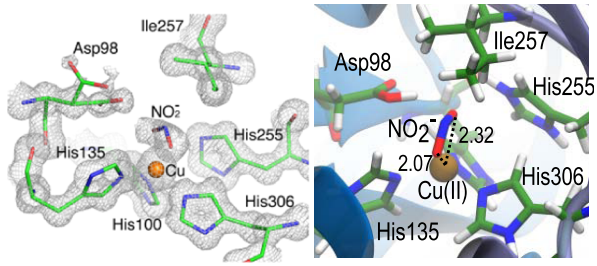

Figure 4. Experimental MSOX data set ds1 (left) with Cu−O distances of 1.97 and 2.03 Å, and optimized QM/MM (right) structures showing equivalent orientations of the top-hat NO_2^- bound to Cu(II) at the T2Cu site, with distances in Å.

of NO_2^- bound in the bidentate top-hat orientation to oxidized Cu(II) at the T2Cu site. Further analysis of the geometries according to the method of ref 47 for different protonation states of Asp_{CAT} and His_{CAT} is provided in the SI, Table S1.

Since NO_2^- could potentially take up a proton[c] to form HNO_2, a change that would not be visible in the electron density maps and resulting structures, we also performed a QM/MM optimization of HNO_2 bound to T2Cu(II). This resulted in the formation of top-hat nitrite-bound NO_2^- geometry along with the transfer of a proton from HNO_2 to the Asp_{CAT} (which becomes doubly protonated in the case of Asp98p). Asp_{CAT} would eventually lose its proton to water in the same water channel or to His_{CAT}, depending on the nature of the electrostatic potential of the local microenvironment. A representative optimized structure of T2Cu(II)-bound HNO_2 is given in Figure S1 in the SI.

We also considered whether the top-hat structure could correspond to NO_2^- binding to T2Cu(I). However, all optimizations of NO_2^- starting in the Cu(I) oxidation state resulted in geometries other than the observed bidentate top-hat (vide infra). Optimizations of HNO_2 in the same oxidation state also produced structures that did not correspond to the experimental observations.

4.1.2. Snapshot 2: Side-on Orientation of NO_2^-. The second observed intermediate (ds2) corresponds to a side-on orientation of NO_2^-, where all of the nitrite atoms are near-equidistant from Cu with Cu−O distances of 1.98 and 2.01 Å and a Cu−N distance of 2.15 Å (Figure 3B). All T2Cu(II) state optimizations starting from the side-on geometry returned to the top-hat state irrespective of the protonation states of Asp_{CAT} and His_{CAT}, indicating that side-on NO_2^- binding is not favorable in the Cu(II) state (see Table S1).

We next considered the Cu(I) oxidation state. Two probable scenarios were considered: (i) reduction prior to proton transfer to NO_2^-, representing NO_2^- bound to Cu(I) at the T2Cu site, and (ii) proton transfer followed by reduction, representing HNO_2 bound to Cu(I) at the T2Cu site. QM/MM geometry optimizations with the HNO_2 ligand bound to Cu(I) yielded geometries of the ligand that are distinctly different from the experimentally observed ones and hence are

https://doi.org/10.1021/acs.jpcb.1c03661
J. Phys. Chem. B 2021, 125, 9102−9114

not representative of the observed side-on intermediate, and so are not considered further. Thus, the only remaining possibility is Cu(I) with NO_2^- bound in the active site. Optimization of Cu(I)−NO_2^- was evaluated from MSOX-observed side-on NO_2^- as well as from the two alternative top-hat NO_2^--bound geometries seen in the MSOX structures. In contrast to the Cu(II) case, and consistent with our previous DFT calculations,[27] we were able to find a side-on NO_2^- minimum on the Cu(I) potential energy surface (Figure 5A). We also

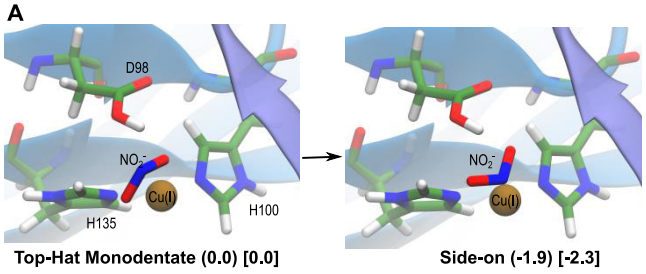

Figure 5. (A) Intermediates with NO_2^- bound to reduced Cu(I) found by QM/MM calculations. Energies in kcal/mol relative to Cu(I) top-hat monodentate calculated at the B3LYP-D3/def2-TZVP(Cu):def2-SVP(all):CHARMM level are given in parentheses, while ΔG values in kcal/mol are provided in square brackets. (B) Calculated NEB pathway from the monodentate top-hat Cu(I) geometry to the side-on Cu(I) intermediate.

found a second minimum that resembles a top-hat geometry but in a monodentate binding mode involving one of the oxygen atoms (Figure 5A). Steepest descent (SD) optimizations starting from the Cu(II) top-hat structure revealed a barrierless path to the "monodentate top-hat" minimum on the Cu(I) surface, suggesting that this orientation is an intermediate on the path to the side-on orientation. We next carried out a CI-NEB minimization between the monodentate top-hat and side-on endpoints, with further refinement of the transition state using the dimer method. These calculations indicated that the formation of side-on from top-hat monodentate geometry occurs via a very small barrier (0.5 kcal/mol), as shown in Figure 5B, suggesting that any top-hat monodentate structure would be transient and so unlikely to be captured and observed by crystallography, even in a high-throughput MSOX series.

The MSOX data series unambiguously identifies the side-on orientation of NO_2^- as an intermediate. However, it should be noted that the calculated QM/MM Cu(I) potential energy surface is complex and we identified two further bound orientations of NO_2^- with similar energies: an N-bound orientation and a "reverse side-on" geometry (where N and O are in a plane, but N is pointing away from Asp_{CAT}, His_{CAT}, and Ile257). In other words, in this reverse scenario, NO_2^- is flipped to an orientation opposite to that observed in the MSOX structure (see Figure S2 for these additional orientations and Table S2 for energetics and geometrical parameters defining these intermediates). As these orientations are not observed experimentally, the MSOX reference data allows us to rule them out as important intermediates on the reaction path in the crystal. This is particularly important as the QM/MM calculations are unable to discriminate satisfactorily between the competing orientations, with the energy ordering of each intermediate dependent on the functional used (for the results of comparable calculations using PBE, PBE0, and B2PLYP, see Table S3). No substantial barriers to accessing the other orientations were observed via CI-NEB calculations (see Figure S3). Calculated entropic corrections based on a vibrational frequency analysis favor the side-on orientation over the N-bound and reverse side-on orientations, but the differences are not sufficiently large to change the overall order (for details, see Table S4). Nevertheless, despite these limitations of the DFT methods used, the calculations are sufficient to unambiguously assign the side-on snapshot to the Cu(I) oxidation state.

4.2. Nitric Oxide Formation in Crystalline *Ac*NiR.

4.2.1. Snapshot 3: NO Bound to T2Cu. The third structure observed in the MSOX data is the NO product. The MSOX structure (ds18 from the series, Figure 3C) reveals a side-on NO bound to T2Cu consistent with the observation of side-on NO binding in all CuNiR crystal structures to date. We aimed to achieve an understanding of how the observed side-on Cu(I) nitrite intermediate in snapshot 2 is reduced to NO through QM/MM calculations. Proton transfer to reduced Cu(I) NO_2^- would lead to conversion of NO_2^- to NO and H_2O, thereby completing the reductive mechanism. Recent neutron diffraction studies on the resting state of *Ac*NiR have indicated the possibility of a deprotonated Asp_{CAT} and a possibility of His_{CAT} being in either the protonated or deprotonated state.[26] The protonation states of these residues on NO_2^- binding are elusive and require further investigation. However, two protons are required for the turnover of NO_2^- to NO so we use the common hypothesis that the proton is transferred from Asp_{CAT} to an NO_2^- oxygen,[23] and the Asp_{CAT} could in turn be protonated by His_{CAT} or from water in the water channel. Rather than providing the explicit pathway of proton transfer necessary for the reduction, we are using His_{CAT} as a possible proton donor to Asp_{CAT}.[23] The crystal water that bridges Asp_{CAT} and His_{CAT} via a hydrogen bond participates in the proton relay from His_{CAT} to Asp_{CAT}. Guided by the MSOX data, we started with the side-on NO_2^- structure, bound to Cu(I) according to our modeling, and optimized it after protonation of the nitrite, without altering the initial protonation states of Asp_{CAT} and His_{CAT} (the system used is Asp98p-Hsp) (Figure 6). The optimization leads to barrierless scission of HNO_2 to NO and OH, while both remain coordinated to Cu giving a penta-coordinated geometry at the T2Cu site. Mulliken charges indicate an $NO^{\delta+}$ and $OH^{\delta-}$ species. A proton transfer [with a barrier of 8.9 kcal/mol calculated using the dimer method, refined from the NEB pathway in the SI, Figure S4] from His_{CAT} to $OH^{\delta-}$ via Asp_{CAT} and bridging water leads to NO and H_2O bound to T2Cu. The reductive pathway leading to the formation of NO bound to T2Cu is provided in Figure 6. Reoptimizing the NO-bound structure after deleting OH^-/H_2O manually resulted in a Cu−N−O angle of around 113° resembling the side-on NO

https://doi.org/10.1021/acs.jpcb.1c03661
J. Phys. Chem. B 2021, 125, 9102−9114

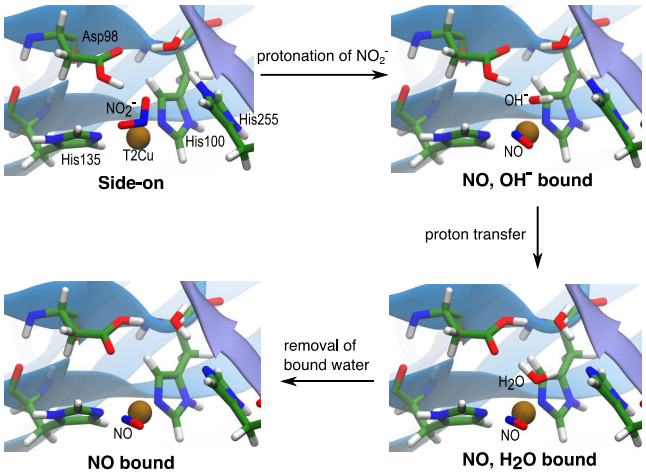

Figure 6. Pathway to the formation of NO-bound T2Cu from side-on NO_2^- bound to reduced Cu(I) via protonation.

orientation observed in MSOX (Figure 7 and Table 1). Mulliken charge analysis of the nitric oxide product indicates an electronic configuration of Cu(I)−NO^+.

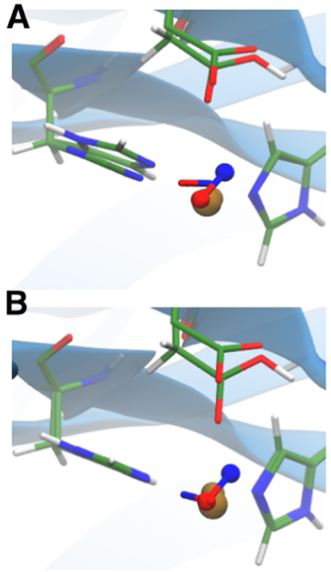

Figure 7. Comparison of experimental and computed NO-bound structures: (A) MSOX (ball and stick) with QM/MM optimized structure from crystal NO (MSOX structure) (sticks); (B) MSOX (ball and stick) with QM/MM crystal structures resulting from the reduction of NO_2^- (stick).

Table 1. Geometric Parameters of NO Intermediates Obtained from Directly Optimizing NO-Bound MSOX Structures, the Crystalline Mechanistic Pathway, and the MSOX Structure[a]

NO intermediates	distances (Å) Cu−N, Cu−O	Cu−N−O angle (deg)
optimized from NO-bound MSOX structure	1.82, 2.74	136.19
NO intermediate from crystalline reaction pathway	1.96, 2.60	112.69
experimental MSOX structure	1.89, 2.22	88.35

[a]The system studied is Asp98p-Hsd considering His_{CAT} as the second proton transfer.

The orientation of NO in the optimized NO-bound structure obtained via the reduction pathway, however, is different from the observed MSOX intermediate, see Figure 7. Again, this likely reflects the complexity of the calculated potential energy surface, with multiple NO-bound local minima. For comparison, we have also optimized the reference MSOX NO-bound structure. The optimized NO structure resulted in a Cu−N−O angle of 136° compared to 88° observed in the crystal structure (see Table 1), again suggesting that the different orientations of NO are too subtle and close in energy to be discriminated by the DFT methods used.

For completeness, we also considered reaction paths beginning from intermediates, which were only observed on the computational potential energy surface and not by the experiment and found that similar paths were taken in each case. For further details, see the SI, page S5.

4.3. Nitrite Reduction in Solvated *Ac*NiR. To ensure that a representative sample of MD snapshots was investigated by QM/MM modeling of the T2Cu site, six starting structures were considered. Four of these are based on differences in water interactions with NO_2^- and Asp_{CAT}: (i) no water interacting at the active site, (ii) water interacting with NO_2^- only, (iii) water interacting with Asp_{CAT}, and (iv) water interacting with both NO_2^- and Asp_{CAT}. The remaining two structures, with no water interacting in the active site, were selected for the position of His_{CAT} and Ile257: (v) His_{CAT} H-bonded to NO_2^- and (vi) His_{CAT} and Ile257 orientations close to the crystal structure. In all of these snapshots, the water bridging the Asp_{CAT} and His_{CAT} via H-bond is maintained. These snapshots were all taken from the last 5 ns of the 25 ns MD production run and QM/MM optimizations were performed on them. The results for both oxidation states were similar to those observed for QM/MM optimizations using the crystal geometry. In particular, the Cu(II) state for all of the snapshots always yielded a bidentate top-hat NO_2^-geometry without exception (Figure 8 and Table S5), a

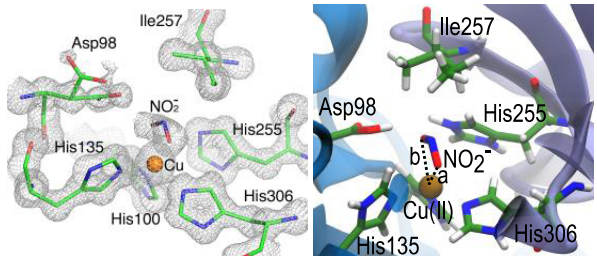

Figure 8. Representative structure of Cu(II)−NO_2^- bidentate top-hat intermediate from the solvated system. The two Cu−O distances, *a* (Å) = 2.04 ± 0.01 and *b* (Å) = 2.40 ± 0.03.

configuration that matches the observed MSOX initial ds1 structure. For the Cu(I) state, we observed a complex landscape analogous to that seen in the crystal QM/MM calculations, with multiple orientations of NO_2^- bound at the T2Cu(I) site, all close in energy. The geometric parameters representing the NO_2^- orientation of all of these intermediates for all of the chosen snapshots are given in Table S5. Snapshot (i) was then chosen for further investigation and the top-hat NO_2^--bound Cu(II) state was reduced to the Cu(I) state using a steepest descent optimizer. Since *Ac*NiR is a homotrimeric protein with a T2Cu site formed at the interface of adjacent monomers, there are three independent T2Cu sites (denoted

https://doi.org/10.1021/acs.jpcb.1c03661
J. Phys. Chem. B 2021, 125, 9102−9114

A, B, and C). Thus, three independent simulations of reduction were performed on the selected snapshot structure. The relative energies of the intermediates in all subunits are provided in Table 2, while absolute energies and geometrical parameters are provided in Table S6. Figure 9 depicts the structures and energetics of one of the SD optimized Cu(I)−NO_2^--bound intermediates, and the rest are provided in Figure S6 of the SI. The results indicate that N-bound Cu(I)−NO_2^- is the thermodynamically most stable structure in all three T2Cu sites. The three sites, however, reveal energetic differences in the distribution of the intermediates: in T2CuA, the side-on and reverse side-on intermediates are isoenergetic and the N-bound only marginally the most stable by less than 1 kcal/mol. The results are similar for T2CuB, albeit the energy differences are greater than those observed for T2CuA. In T2CuC, however, there is a significant energy difference (>7 kcal/mol) between the side-on intermediate and that of the reverse side-on and N-bound intermediates. Interestingly in this unit, a water molecule is close to the bound NO_2^-, whereas, in the other two, this water molecule is absent (see Figure S6).

Table 2. Relative Energies (Calculated at B3LYP-D3/def2-TZVP(Cu):def2-SVP(all):CHARMM) and Geometric Parameters for the Optimized Cu(I)−NO_2^- Intermediates on the Three Subunits (ABC) of the Chosen Snapshot Discussed in the Text[a]

nitrite intermediates		monodentate top-hat	side-on	N-bound	reverse side-on
chain A	ΔE (kcal/mol)	0.0	−4.3	−5.2	−4.5
chain B	ΔE (kcal/mol)	0.0	−1.6	−4.3	−2.3
chain C	ΔE (kcal/mol)	0.0	−1.2	−8.5	−6.4

[a]The relative energies of the intermediates are calculated with respect to the monodentate top-hat intermediate. Absolute energies are provided in Table S6.

CI-NEB profiles were calculated between the monodentate top-hat NO_2^--bound intermediate and the others in the same way as for the crystalline state, and again the barriers to transition were negligible (see Figure S7). The differences in pathways and the distribution of intermediates in different subunits of the same snapshot confirm the shallow nature of the complex energy landscape of Cu(I)-bound NO_2^- intermediates. These observations further suggest that subtle differences in the microenvironment can potentially change the distribution of the intermediates as well as the pathway of their formation.

The QM/MM optimizations of representative snapshots from the other protonation states of Asp_{CAT} and His_{CAT}, i.e., Asp98p-Hsd and Asp98-Hsp, resulted in a bidentate top-hat orientation of NO_2^- bound to Cu(II) state and a complex

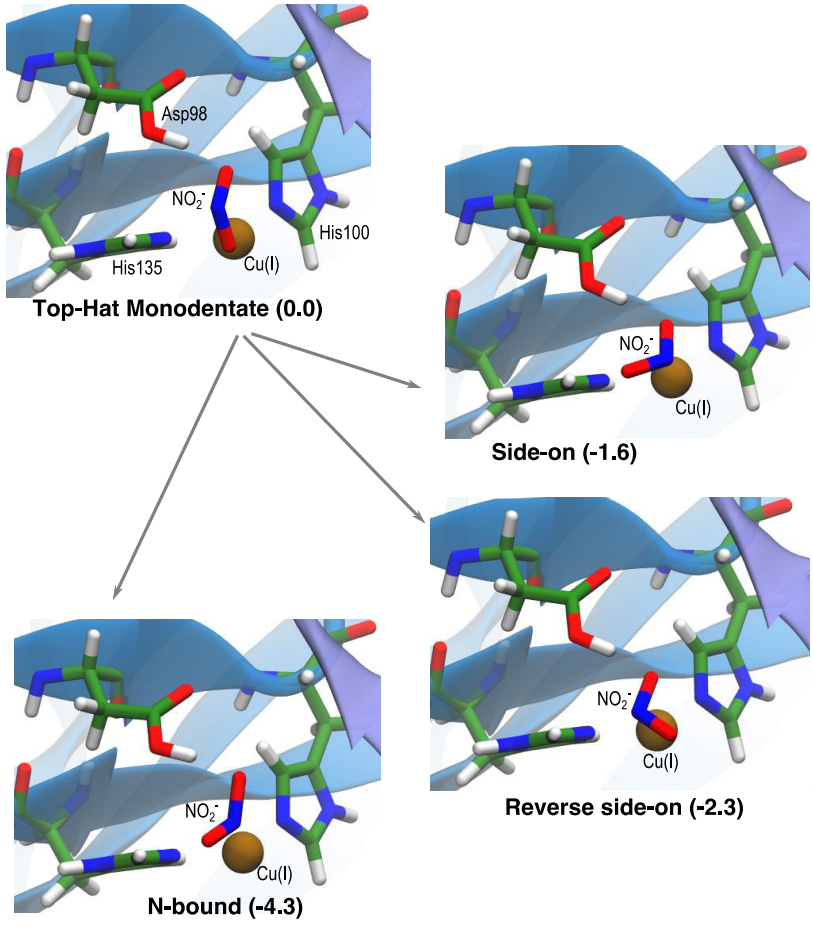

Figure 9. All of the intermediates observed with NO_2^- bound to reduced Cu(I) in one of the T2Cu unit (chain B) in solvated *Ac*NiR. The B3LYP-D3/def2-TZVP(Cu):def2-SVP(all):CHARMM energies in kcal/mol relative to Cu(I) top-hat monodentate are given in parentheses.

https://doi.org/10.1021/acs.jpcb.1c03661
J. Phys. Chem. B 2021, 125, 9102−9114

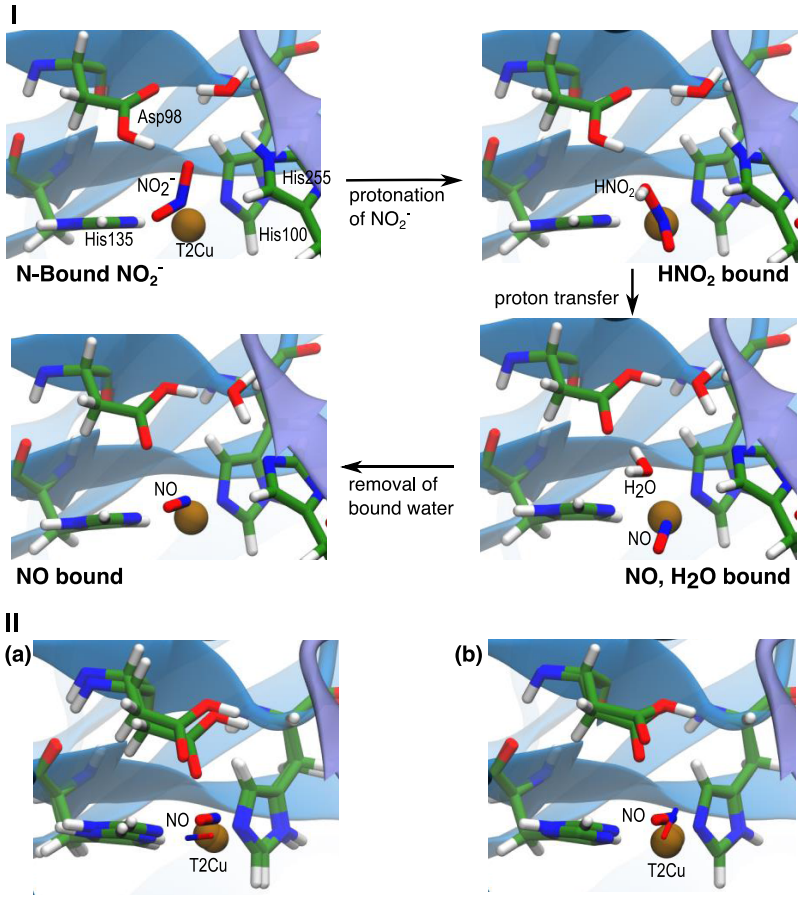

Figure 10. (I) Formation of NO from NO_2^- N-bound to reduced Cu(I) via protonation in the solvated system. (II, a) Overlay of the resultant NO-bound intermediate with the similarly obtained NO structure from the reductive mechanism in the crystal system; (II, b) overlay of the same to the MSOX-observed NO structure.

landscape analogous to that seen for the Asp98p-Hsp system with multiple orientations of NO_2^- bound at the T2Cu(I) site. The geometric parameters for NO_2^- bound to both Cu(II) and Cu(I) for these protonation states are provided in Table S7.

As in the crystal system, we used Asp_{CAT} and His_{CAT} as the proton source to protonate NO_2^- bound to reduced Cu, to yield NO. We again also carried out the protonation of NO_2^--bound Cu(I) in all of the intermediates of the chosen snapshot (i) without altering the initial protonation states of Asp_{CAT} and His_{CAT} (the system used is Asp98p-Hsp). This step was followed by optimization. For the solvated system, the N-bound intermediate was favored. Interestingly, on protonation, N-bound intermediates initially formed an N-bound HNO_2 intermediate which was poised to accept a second proton from His_{CAT}, via the bridging water and Asp_{CAT}, to form NO and water (which remained H-bonded to the nearby Asp_{CAT}) (Figure 10I). Removal of the water after scission of NO_2^- by protonation of N-bound structures (in all three T2Cu sites) resulted in an obliquely bound NO (Figure 10I). The average distances and the Cu−N−O angle for all of the units for the snapshot studied were: Cu−N: 1.81 Å (±0.02), Cu−O: 2.76 Å (±0.01), and Cu−N-O: 138.93° (±3.38). Comparison of the similarly reduced NO from side-on NO_2^- starting from the crystal system reveals that the NO orientation is almost orthogonal (Figure 10II-a); however, comparing it with the original MSOX structure, the orientation of NO is in alignment to it (Figure 10II-b), although the Cu−N−O angle is ∼50° more oblique relative to the observed angle of 88.35°. The side-on intermediate on protonation either formed an N-bound HNO_2 structure, as observed in N-bound intermediates, or side-on HNO_2 forming a H-bond with Asp_{CAT}, or formed a dissociated HNO_2 in the active site H-bonded to His135. The reverse side-on intermediates on protonation formed a weakly bound HNO_2 species of the same orientation (with Cu−N and Cu−O1 distances of the order of ∼2.7 Å) and, rarely, an N-bound HNO_2 structure. The monodentate intermediate either collapsed into weakly bound reverse side-on HNO_2 or did not correspond to a structure observed in MSOX. All of the structures of these intermediates are provided in Figure S8.

5. DISCUSSION

MSOX is a powerful tool to observe intermediate structures evolved during a reduction reaction occurring in one crystal and provides a wealth of structural information that is otherwise unavailable via conventional single-structure macromolecular X-ray crystallography. MSOX data for *Ac*NiR at various temperatures (100 K to room temperature) characterized three distinct intermediates along its reaction pathway: a top-hat-bound NO_2^-, a side-on-bound NO_2^-, and a side-on NO that is eventually replaced by water leading back to the resting state of the enzyme.[1,12] Information regarding metal oxidation states in CuNiRs is not revealed by MSOX but can be partially assigned (for the T1Cu chromophore) by parallel in situ spectroscopies.[48] However, the protonation states of titratable residues in the active site or its immediate vicinity are

https://doi.org/10.1021/acs.jpcb.1c03661
J. Phys. Chem. B 2021, 125, 9102−9114

Scheme 1. Schematic of the Reduction of NO_2^- to NO at the T2Cu Site Obtained from QM/MM Calculations in the Crystal System

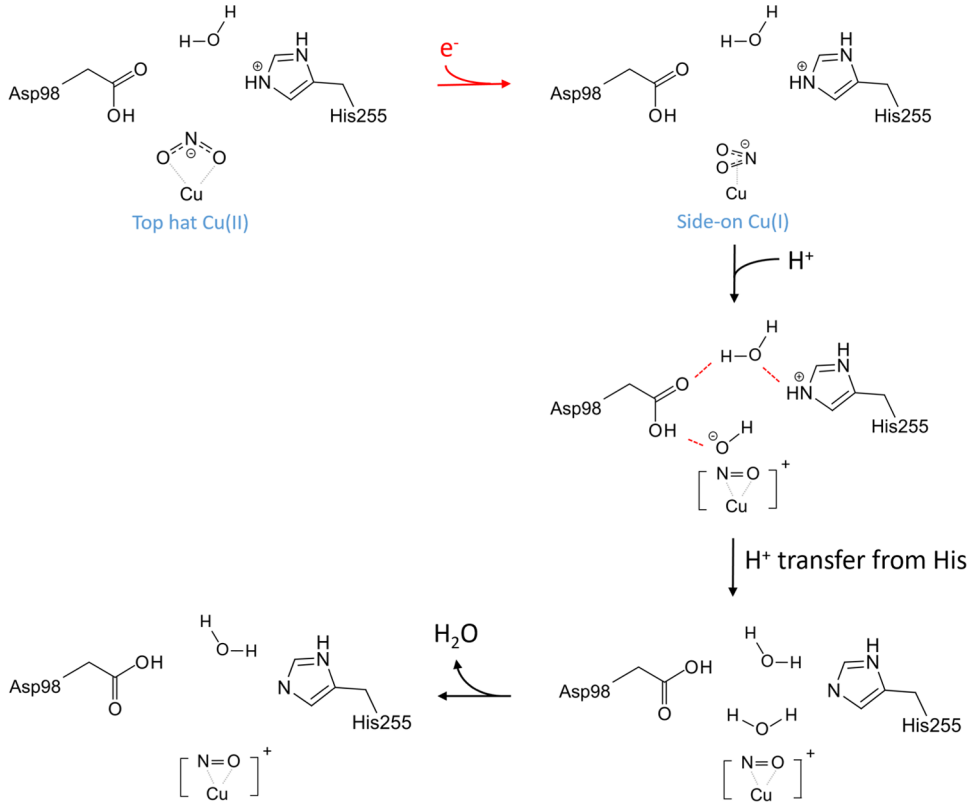

not determined. In this paper, we have shown how QM/MM studies can be combined with MSOX structures to model observed states, to reveal transient and potentially hidden states, and so obtain a clearer understanding of the reduction reaction carried out by CuNiRs.

The QM/MM results on the crystal system derived from MSOX show that the observed top-hat orientation of NO_2^- at the T2Cu site corresponds exclusively to the Cu(II) state (Figure 4). Furthermore, the possibility that NO_2^- is protonated as it enters the active site and binds to T2Cu(II) as HNO_2 is revealed to be unfeasible by our QM/MM calculations.

The second MSOX intermediate, the side-on-bound NO_2^-, is ruled out as belonging to the Cu(II) oxidation state as the optimized structure with this metal oxidation state always reverted back to a top-hat geometry. This is in apparent contradiction to recent serial femtosecond rotational crystallography (SF-ROX) and neutron structures of *Ac*NiR, which indicate the presence of NO_2^- in both side-on and top-hat binding modes in the oxidized state.[26] It was suggested that the flip between top-hat and side-on modes is controlled by changes to internal pH. It is hard to reconcile this with our computational results for the MSOX structures, where we found that Cu(II)-nitrite cannot assume a side-on orientation with any combination of protonation states of Asp_{CAT} and His_{CAT}. One possibility is that the orientation is sensitive to subtle differences between the SF-ROX and MSOX structures. For comparison in a three-domain CuNiR Asp_{CAT} to Asn mutant, *Rp*NiR, an L-shaped N-bound nitrite orientation that resembles a distorted side-on orientation was obtained with the Cu(II) state,[47,49] and ordinary dynamicity in the active site could modulate the nitrite orientation too. Another possibility is that the protonation states of other residues besides Asp_{CAT} and His_{CAT} are important in determining the nitrite orientation, although it is not obvious which other residues may be responsible.

In the Cu(I) state, side-on-bound NO_2^- can be formed, and so we assign this oxidation state unambiguously to the observed side-on intermediate. Although the nitrite could in principle be protonated (as this would not be observable in the MSOX snapshot), attempts to optimize HNO_2 bound to Cu(I) resulted in structures inconsistent with any MSOX observations, from which we infer that the nitrite is unprotonated at this stage. Other orientations of bound nitrite (N-bound and reverse side-on) are also minima on the QM/MM energy surface, but as they too do not correspond to experimental observations, they can similarly be ruled out as intermediates on the reaction path. Here, the value of MSOX can be appreciated as it greatly reduces the number of potential reaction paths that need to be considered on a complex energy surface. The limitation of DFT methods to discriminate between the orientations is not overcome by changing the functional or by applying simple entropic corrections based on a vibrational frequency analysis (future work will consider whether more sophisticated free energy calculations, e.g., QM/MM free energy perturbation methods, may resolve these discrepancies). Nevertheless, the combination of computational and experimental data reveals unambiguously both the orientation and oxidation state of this intermediate.

Protonation of the side-on Cu(I)-bound NO_2^- led to the production of NO and OH, which following the second proton transfer from the implicated active site residues Asp_{CAT} and His_{CAT} leads to formation of NO and water coordinated to T2Cu. Displacement of H_2O leads to the formation of the

https://doi.org/10.1021/acs.jpcb.1c03661
J. Phys. Chem. B 2021, 125, 9102−9114

third observed MSOX intermediate, NO bound to T2Cu. The full reaction mechanism is shown in Scheme 1.

The MSOX NO intermediate is fully side-on; however, the QM/MM optimized NO-bound structures (both QM/MM optimization of the NO-bound MSOX structure and NO obtained via the QM/MM reduction mechanism) illustrated a range of orientations with the Cu−N−O angle varying between 110 and 136°, which we denote as "oblique side-on" (Figure 7). Again we conclude that unambiguously defining the precise orientation of binding is likely to be beyond the capabilities of a DFT-based computational approach, but this does not affect the overall reaction mechanism.

Once we had established the electronic states of the intermediates as observed in the crystal state of MSOX data with QM/MM calculations, we compared with modeled behavior of the enzyme in its solvated state. The top-hat orientation again corresponded only to a Cu(II) state, and hence it can be concluded that the first observed top-hat orientation is the initial structure of NO_2^- bound to T2Cu in *Ac*NiR irrespective of whether the enzyme is in crystal or in solution. In the Cu(I) state, the side-on NO_2^- orientation is one among another three observed intermediates. There is, however, a difference in the distribution of energies of these intermediates compared to the crystal system. In the solvated system, the N-bound intermediate is the lowest in energy with side-on and reverse side-on modes close in energy to it. The N-bound intermediate on proton transfer yielded an obliquely bound NO, with a Cu−N−O angle of ∼138.93 ± 3.38° compared to ∼110° in the crystal system and 88° observed in the MSOX structure. However, it is not possible to conclude from this that the N-bound intermediate is the only important orientation in the solvated reaction path, given the limitations of DFT to discriminate between the orientations as already observed in the crystal case. More sophisticated free energy approaches are therefore required to evaluate the relative importance of each orientation in the solvated case, which we will consider in future work. This contrasts with MSOX-guided QM/MM calculations for the crystal reaction, where we know unambiguously that the side-on orientation is the intermediate on the reaction path thanks to the experimental reference data, and so a more sophisticated QM/MM free energy approach is not required. Moreover, the fact that the reaction mechanism is overall very similar for both the crystal and solvated calculations suggests that the reaction in the crystal protein is a good model for the behavior of the in vivo enzyme.

6. CONCLUSIONS

The combination of MSOX serial crystallography and QM/MM modeling provides a detailed insight into the nitrite reduction mechanism in crystalline *Ac*NiR. Guided by the MSOX data series, QM/MM calculations unambiguously assign the Cu(II) oxidation state to the initial top-hat orientation of nitrite bound to T2Cu, and Cu(I) to the subsequent side-on orientated structure, in line with previous DFT calculations on model complexes. The QM/MM calculations further indicate that the bound species at both points is NO_2^- rather than HNO_2. The reaction path to the third structure in the MSOX data series, featuring bound NO, has been mapped, with protonation resulting in a barrierless transition to bound NO and OH, and a further protonation from His_{CAT} via Asp_{CAT} and a bridging water to form H_2O, which then is lost leaving the bound Cu(I)−NO^+ complex.

QM/MM calculations also facilitate the comparison of the reaction in the crystal with the same process in a solvated environment. The change in environment does not result in any differences in the Cu oxidation state, with the top-hat structure still corresponding to Cu(II) and all other orientations corresponding to Cu(I). Formation of HNO_2 is also ruled out again during the initial stages of the reaction. A notable difference in the solvated environment is that the N-bound nitrite orientation is computed to be the most stable, although side-on and reverse side-on are also present and close in energy just as they are in the crystal and should not be ruled out as intermediates on the reaction path. Regardless of the nitrite orientation, the overall reaction proceeds in much the same way as in the crystal, with protonation of nitrite resulting in an HNO_2 ligand that can accept a second proton from the catalytic residues to form NO and water.

The combination of QM/MM simulation with MSOX reference data is a powerful means to characterize the reaction mechanism for the nitrite reduction taking place in a crystal environment, with QM/MM simulations providing important additional information that cannot be observed experimentally, while MSOX snapshots constrain the space of possible reaction paths, thereby guiding QM/MM simulations from intermediate to intermediate. We expect this combination to be equally applicable to other crystal redox systems.

■ ASSOCIATED CONTENT

Supporting Information

The Supporting Information is available free of charge at https://pubs.acs.org/doi/10.1021/acs.jpcb.1c03661.

Further details of geometrical parameters, optimized structures, intermediate energies, nudged elastic band pathways, and thermal and entropic corrections for NO_2^-, HNO_2, and NO bound to T2Cu in the crystal and solvated systems (PDF)

■ AUTHOR INFORMATION

Corresponding Authors

Richard W. Strange − *School of Life Sciences, University of Essex, Colchester, Essex CO4 3SQ, United Kingdom*; Email: r.strange@essex.ac.uk

Thomas W. Keal − *Scientific Computing Department, STFC Daresbury Laboratory, Warrington, Cheshire WA4 4AD, United Kingdom*; orcid.org/0000-0001-8747-3975; Email: thomas.keal@stfc.ac.uk

Authors

Kakali Sen − *School of Life Sciences, University of Essex, Colchester, Essex CO4 3SQ, United Kingdom; Scientific Computing Department, STFC Daresbury Laboratory, Warrington, Cheshire WA4 4AD, United Kingdom*; orcid.org/0000-0003-3135-3688

Michael A. Hough − *School of Life Sciences, University of Essex, Colchester, Essex CO4 3SQ, United Kingdom*; orcid.org/0000-0001-7377-6713

Chin Yong − *Scientific Computing Department, STFC Daresbury Laboratory, Warrington, Cheshire WA4 4AD, United Kingdom*

Complete contact information is available at: https://pubs.acs.org/10.1021/acs.jpcb.1c03661

https://doi.org/10.1021/acs.jpcb.1c03661
J. Phys. Chem. B 2021, 125, 9102−9114

Notes

The authors declare no competing financial interest.

■ ACKNOWLEDGMENTS

The authors would like to thank our former group members Demet Kekilli (Swiss Light Source) and Sam Horrell (Diamond Light Source) for their invaluable contributions to establishing the experimental protocols and methods for MSOX. The authors thank Samar Hasnain, Robert Eady, and Svetlana Antonyuk at the University of Liverpool for helpful discussions over many years on the structure and chemistry of copper nitrite reductases. The authors are grateful for STFC computing resources provided by the Scientific Computing Department's SCARF cluster and Hartree Centre's Iden and Napier clusters. The work was supported by BBSRC grants BB/M022714/1 (MAH), BB/M020924/1 (RWS), and BB/M022390/1 (TWK).

■ ABBREVIATIONS

CuNiR, copper nitrite reductase; MSOX, multiple structures from one crystal; QM/MM, quantum mechanics/molecular mechanics

■ ADDITIONAL NOTES

[a]The ambient temperatures at the synchrotron beamlines used were 22.5 °C (Swiss Light Source) and 21 °C (Diamond Light Source).
[b]Derived from data sets ds1, ds2, and ds18, respectively.
[c]From water in the solvent/substrate accessible channel or from the active site residues Asp_{CAT} and His_{CAT}, both of which are implicated in the proton transfer network.

■ REFERENCES

(1) Horrell, S.; Antonyuk, S. V.; Eady, R. R.; Hasnain, S. S.; Hough, M. A.; Strange, R. W. Serial crystallography captures enzyme catalysis in copper nitrite reductase at atomic resolution from one crystal. *IUCrJ* **2016**, *3*, 271−281.
(2) Ebrahim, A.; Moreno-Chicano, T.; Appleby, M. V.; Chaplin, A. K.; Beale, J. H.; Sherrell, D. A.; Duyvesteyn, H. M. E.; Owada, S.; Tono, K.; Sugimoto, H.; et al. Dose-resolved serial synchrotron and XFEL structures of radiation-sensitive metalloproteins. *IUCrJ* **2019**, *6*, 543−551.
(3) Garman, E. F.; Weik, M. Radiation Damage in Macromolecular Crystallography. In *Protein Crystallography: Methods and Protocols*; Wlodawer, A.; Dauter, Z.; Jaskolski, M., Eds.; Springer: New York, NY, 2017; pp 467−489.
(4) Schlichting, I.; Berendzen, J.; Chu, K.; Stock, A. M.; Maves, S. A.; Benson, D. E.; Sweet, R. M.; Ringe, D.; Petsko, G. A.; Sligar, S. G. The catalytic pathway of cytochrome P450cam at atomic resolution. *Science* **2000**, *287*, 1615−1622.
(5) Kekilli, D.; Moreno-Chicano, T.; Chaplin, A. K.; Horrell, S.; Dworkowski, F. S. N.; Worrall, J. A. R.; Strange, R. W.; Hough, M. A. Photoreduction and validation of haem-ligand intermediate states in protein crystals by in situ single-crystal spectroscopy and diffraction. *IUCrJ* **2017**, *4*, 263−270.
(6) Pompidor, G.; Dworkowski, F. S. N.; Thominet, V.; Schulze-Briese, C.; Fuchs, M. R. A new on-axis micro-spectrophotometer for combining Raman, fluorescence and UV-Vis absorption spectroscopy with macromolecular crystallography at the Swiss Light Source. *J. Synchrotron Radiat.* **2013**, *20*, 765−776.
(7) Dworkowski, F. S. N.; Hough, M. A.; Pompidor, G.; Fuchs, M. R. Challenges and solutions for the analysis of in situ, *in crystallo* micro-spectrophotometric data. *Acta Crystallogr., Sect. D: Biol. Crystallogr.* **2015**, *71*, 27−35.
(8) Owen, R. L.; Paterson, N.; Axford, D.; Aishima, J.; Schulze-Briese, C.; Ren, J.; Fry, E. E.; Stuart, D. I.; Evans, G. Exploiting fast detectors to enter a new dimension in room-temperature crystallography. *Acta Crystallogr., Sect. D: Biol. Crystallogr.* **2014**, *70*, 1248−1256.
(9) Beitlich, T.; Kühnel, K.; Schulze-Briese, C.; Shoeman, R. L.; Schlichting, I. Cryoradiolytic reduction of crystalline heme proteins: analysis by UV-Vis spectroscopy and X-ray crystallography. *J. Synchrotron Radiat.* **2007**, *14*, 11−23.
(10) Antonyuk, S. V.; Hough, M. A. Monitoring and validating active site redox states in protein crystals. *Biochim. Biophys. Acta, Proteins Proteomics* **2011**, *1814*, 778−784.
(11) Gerstel, M.; Deane, C. M.; Garman, E. F. Identifying and quantifying radiation damage at the atomic level. *J. Synchrotron Radiat.* **2015**, *22*, 201−212.
(12) Horrell, S.; Kekilli, D.; Sen, K.; Owen, R. L.; Dworkowski, F. S. N.; Antonyuk, S. V.; Keal, T. W.; Yong, C. W.; Eady, R. R.; Hasnain, S. S.; et al. Enzyme catalysis captured using multiple structures from one crystal at varying temperatures. *IUCrJ* **2018**, *5*, 283−292.
(13) Senn, H. M.; Thiel, W. QM/MM Methods for Biomolecular Systems. *Angew. Chem., Int. Ed.* **2009**, *48*, 1198−1229.
(14) Zheng, J.; Altun, A.; Thiel, W. Common System Setup for the Entire Catalytic Cycle of Cytochrome $P450_{cam}$ in Quantum Mechanical/Molecular Mechanical Studies. *J. Comput. Chem.* **2007**, *28*, 2147−2158.
(15) Zhang, Y.; Kua, J.; McCammon, J. A. Influence of Structural Fluctuation on Enzyme Reaction Energy Barriers in Combined Quantum Mechanical/Molecular Mechanical Studies. *J. Phys. Chem. B* **2003**, *107*, 4459−4463.
(16) Knowles, R. Denitrification. *Microbiol. Rev.* **1982**, *46*, 43−70.
(17) Zumft, W. G. Cell biology and the molecular basis of denitrification. *Microbiol. Mol. Biol. Rev* **1997**, *61*, 533−616.
(18) Horrell, S.; Kekilli, D.; Strange, R. W.; Hough, M. A. Recent structural insights into the function of copper nitrite reductases. *Metallomics* **2017**, *9*, 1470−1482.
(19) Li, Y.; Hodak, M.; Bernholc, J. Enzymatic Mechanism of Copper-Containing Nitrite Reductase. *Biochemistry* **2015**, *54*, 1233−1242.
(20) Maekawa, S.; Matsui, T.; Hirao, K.; Shigeta, Y. Theoretical Study on Reaction Mechanisms of Nitrite Reduction by Copper Nitrite Complexes: Toward Understanding and Controlling Possible Mechanisms of Copper Nitrite Reductase. *J. Phys. Chem. B* **2015**, *119*, 5392−5403.
(21) Lintuluoto, M.; Lintuluoto, J. M. DFT Study on Enzyme Turnover Including Proton and Electron Transfers of Copper-Containing Nitrite Reductase. *Biochemistry* **2016**, *55*, 4697−4707.
(22) Lintuluoto, M.; Lintuluoto, J. M. DFT Study on Nitrite Reduction Mechanism in Copper-Containing Nitrite Reductase. *Biochemistry* **2016**, *55*, 210−223.
(23) Lintuluoto, M.; Lintuluoto, J. M. Intra-electron transfer induced by protonation in copper-containing nitrite reductase. *Metallomics* **2018**, *10*, 565−578.
(24) Leferink, N. G. H.; Han, C.; Antonyuk, S. V.; Heyes, D. J.; Rigby, S. E. J.; Hough, M. A.; Eady, R. R.; Scrutton, N. S.; Hasnain, S. S. Proton-coupled electron transfer in the catalytic cycle of Alcaligenes xylosoxidans copper-dependent nitrite reductase. *Biochemistry* **2011**, *50*, 4121−4131.
(25) Hough, M. A.; Eady, R. R.; Hasnain, S. S. Identification of the proton channel to the active site type 2 Cu center of nitrite reductase: structural and enzymatic properties of the His254Phe and Asn90Ser mutants. *Biochemistry* **2008**, *47*, 13547−13553.
(26) Halsted, T. P.; Yamashita, K.; Gopalasingam, C. C.; Shenoy, R. T.; Hirata, K.; Ago, H.; Ueno, G.; Blakeley, M. P.; Eady, R. R.; Antonyuk, S. V.; et al. Catalytically important damage-free structures of a copper nitrite reductase obtained by femtosecond X-ray laser and room-temperature neutron crystallography. *IUCrJ* **2019**, *6*, 761−772.
(27) Sen, K.; Horrell, S.; Kekilli, D.; Yong, C. W.; Keal, T. W.; Atakisi, H.; Moreau, D. W.; Thorne, R. E.; Hough, M. A.; Strange, R. W. Active-site protein dynamics and solvent accessibility in native

https://doi.org/10.1021/acs.jpcb.1c03661
J. Phys. Chem. B 2021, 125, 9102−9114

Achromobacter cycloclastes copper nitrite reductase. *IUCrJ* **2017**, *4*, 495−505.
(28) Olsson, M. H.; Søndergaard, C. R.; Rostkowski, M.; Jensen, J. H. PROPKA3: Consistent Treatment of Internal and Surface Residues in Empirical pKa Predictions. *J. Chem. Theory Comput.* **2011**, *7*, 525−537.
(29) Søndergaard, C. R.; Olsson, M. H.; Rostkowski, M.; Jensen, J. H. Improved Treatment of Ligands and Coupling Effects in Empirical Calculation and Rationalization of pKa Values. *J. Chem. Theory Comput.* **2011**, *7*, 2284−2295.
(30) Dolinsky, T. J.; Czodrowski, P.; Li, H.; Nielsen, J. E.; Jensen, J. H.; Klebe, G.; Baker, N. A. PDB 2PQR: expanding and upgrading automated preparation of biomolecular structures for molecular simulations. *Nucleic Acids Res.* **2007**, *35*, W522−W525.
(31) Ghosh, S.; Dey, A.; Sun, Y.; Scholes, C. P.; Solomon, E. I. Spectroscopic and computational studies of nitrite reductase: proton induced electron transfer and backbonding contributions to reactivity. *J. Am. Chem. Soc.* **2009**, *131*, 277−288.
(32) Sherwood, P.; de Vries, A. H.; Guest, M. F.; Schreckenbach, G.; Catlow, C. R. A.; French, S. A.; Sokol, A. A.; Bromley, S. T.; Thiel, W.; Turner, A. J.; et al. QUASI: A general purpose implementation of the QM/MM approach and its application to problems in catalysis. *J. Mol. Struct.: THEOCHEM* **2003**, *632*, 1−28.
(33) Metz, S.; Kästner, J.; Sokol, A. A.; Keal, T. W.; Sherwood, P. ChemShell-a modular software package for QM/MM simulations. *Wiley Interdiscip. Rev.: Comput. Mol. Sci.* **2014**, *4*, 101−110.
(34) Neese, F. The ORCA program system. *Wiley Interdiscip. Rev.: Comput. Mol. Sci.* **2012**, *2*, 73−78.
(35) Smith, W.; Forester, T. R. DL_POLY_2.0: A general-purpose parallel molecular dynamics simulation package. *J. Mol. Graphics* **1996**, *14*, 136−141.
(36) Kästner, J.; Carr, J. M.; Keal, T. W.; Thiel, W.; Wander, A.; Sherwood, P. DL-FIND: an open-source geometry optimizer for atomistic simulations. *J. Phys. Chem. A* **2009**, *113*, 11856−11865.
(37) Becke, A. D. Density-functional thermochemistry. III. The role of exact exchange. *J. Chem. Phys.* **1993**, *98*, 5648−5652.
(38) Lee, C.; Yang, W.; Parr, R. G. Development of the Colle-Salvetti correlation-energy formula into a functional of the electron density. *Phys. Rev. B* **1988**, *37*, 785−789.
(39) Grimme, S.; Antony, J.; Ehrlich, S.; Krieg, H. A consistent and accurate ab initio parametrization of density functional dispersion correction (DFT-D) for the 94 elements H-Pu. *J. Chem. Phys.* **2010**, *132*, No. 154104.
(40) Weigend, F.; Ahlrichs, R. Balanced basis sets of split valence, triple zeta valence and quadruple zeta valence quality for H to Rn: Design and assessment of accuracy. *Phys. Chem. Chem. Phys.* **2005**, *7*, 3297−3305.
(41) Best, R. B.; Zhu, X.; Shim, J.; Lopes, P. E. M.; Mittal, J.; Feig, M.; MacKerell, A. D. Optimization of the Additive CHARMM All-Atom Protein Force Field Targeting Improved Sampling of the Backbone φ, ψ and Side-Chain $\chi(1)$ and $\chi(2)$ Dihedral Angles. *J. Chem. Theory Comput.* **2012**, *8*, 3257−3273.
(42) Henkelman, G.; Uberuaga, B. P.; Jónsson, H. A climbing image nudged elastic band method for finding saddle points and minimum energy paths. *J. Chem. Phys.* **2000**, *113*, 9901−9904.
(43) Henkelman, G.; Jónsson, H. A dimer method for finding saddle points on high dimensional potential surfaces using only first derivatives. *J. Chem. Phys.* **1999**, *111*, 7010−7022.
(44) Jorgensen, W. L.; Chandrasekhar, J.; Madura, J. D.; Impey, R. W.; Klein, M. L. Comparison of simple potential functions for simulating liquid water. *J. Chem. Phys.* **1983**, *79*, 926−935.
(45) Humphrey, W.; Dalke, A.; Schulten, K. VMD: Visual molecular dynamics. *J. Mol. Graphics* **1996**, *14*, 33−38.
(46) Phillips, J. C.; Braun, R.; Wang, W.; Gumbart, J.; Tajkhorshid, E.; Villa, E.; Chipot, C.; Skeel, R. D.; Kalé, L.; Schulten, K. Scalable molecular dynamics with NAMD. *J. Comput. Chem.* **2005**, *26*, 1781−1802.
(47) Sen, K.; Hough, M. A.; Strange, R. W.; Yong, C. W.; Keal, T. W. A QM/MM Study of Nitrite Binding Modes in a Three-Domain Heme-Cu Nitrite Reductase. *Molecules* **2018**, *23*, No. 2997.
(48) Hough, M. A.; Antonyuk, S. V.; Strange, R. W.; Eady, R. R.; Hasnain, S. S. Crystallography with Online Optical and X-ray Absorption Spectroscopies Demonstrates an Ordered Mechanism in Copper Nitrite Reductase. *J. Mol. Biol.* **2008**, *378*, 353−361.
(49) Dong, J.; Sasaki, D.; Eady, R. R.; Antonyuk, S. V.; Hasnain, S. S. Identification of a tyrosine switch in copper-haem nitrite reductases. *IUCrJ* **2018**, *5*, 510−518.

https://doi.org/10.1021/acs.jpcb.1c03661
J. Phys. Chem. B 2021, 125, 9102−9114